1

2

Endocytosis caused by liquid-liquid phase separation of proteins

4

Louis-Philippe Bergeron-Sandoval[1], Hossein Khadivi Heris[2], Adam G. Hendricks[2], Allen J. Ehrlicher[2], Paul François[3], Rohit V. Pappu[4] and Stephen W. Michnick[1,5*]

Affiliations

[1]Département de Biochimie, Université de Montréal, C.P. 6128, Succursale centre-ville, Montréal, Québec, H3C 3J7, Canada.
[2]Department of Bioengineering, McGill University, 817 Sherbrooke St West, Room 270, Montreal, Quebec, H3A0C3, Canada.
[3]Ernest Rutherford Physics Building, McGill University, 3600 University St, Montreal, Québec, H3A2T8
[4]Department of Biomedical Engineering and Center for Biological Systems Engineering, Washington University in St. Louis, One Brookings Drive, Campus Box 1097, St. Louis, Missouri 63130, USA.
[5]Centre Robert-Cedergren, Bio-Informatique et Génomique, Université de Montréal, C.P. 6128, Succursale centre-ville, Montréal, Québec, H3C 3J7, Canada.

*Correspondence to: S.W.M. (stephen.michnick@umontreal.ca).

21

Summary

23

Clathrin-mediated endocytosis (CME) underlies intra- and extracellular material trafficking in eukaryotes, and is essential to protein metabolism, intercellular signaling, membrane remodeling and other cell regulatory processes. Although CME is usually driven by F-actin polymerization, membrane invagination can also occur through actin independent mechanisms. Here, we show that viscoelastic protein condensates that form via liquid-liquid phase separation at the sites of endocytosis initiation facilitate actin independent CME. The work required to drive membrane invagination is generated by binding energies of the condensate with the membrane and surrounding cytosol. Our findings expand the repertoire of functions associated with protein condensates that form via liquid-liquid phase separation to include their ability to do work at soft interfaces, thus shaping and organizing cellular matter.

Introduction

Evolution has resulted in numerous innovations by which morphogenesis of organisms occurs within limits imposed by physical and chemical constraints on the underlying biochemical processes (Darwin 1859, Thompson 1917). One such process is clathrin-mediated endocytosis (CME) a fundamental mechanism of cell surface membrane receptor turnover and recycling, nutrient uptake and synaptic vesicle regeneration, among others (Conner and Schmid 2003). The mechanism of membrane invagination in CME has most convincingly been demonstrated to be growth of membrane-bound branched actin, however CME has also been shown to occur under conditions where actin polymerization is absent and the mechanisms by which this happens remain unclear (Aghamohammadzadeh and Ayscough 2009, Li, Shao et al. 2015). Here, we demonstrate that membrane invagination can arise from liquid-liquid phase separation (demixing) of proteins with prion-like domains (PLD) from the cytosol (Fig. 1a). Demixing of these proteins results in formation of a droplet (or condensate), which, by virtue of its viscoelastic properties, binds to and deforms plasma membrane and cytosol. Demonstration that phase separated droplets can perform mechanical work expands the repertoire of known functions of protein condensates to include the ability to do work at the droplet interfaces. Similar mechanisms may govern or contribute to other membrane shaping, invagination and budding processes that are involved in the cellular material uptake, secretion, and cell shape remodeling.

In *S. cerevisiae,* the dominant mechanism for vesicle generation in CME is branched actin assembly, which is required to compete against intracellular turgor pressure and membrane tension to drive the invagination of the plasma membrane (Carlsson and Bayly 2014, Dmitrieff and Nedelec 2015). If, however, turgor pressure is eliminated, CME can also occur independent of actin polymerization (Aghamohammadzadeh and Ayscough 2009, Li, Shao et al. 2015). Complementary mechanisms have been proposed to explain actin-independent membrane invagination in CME include intrinsic twisting of the membrane by the clathrin matrix, binding of curved BAR (Bin/Amphiphysin/Rvs) domain-containing proteins (Yu and Schulten 2013), protein domain insertion in the membrane bilayer (Ford, Mills et al. 2002), local relief of turgor pressure (Scher-Zagier and Carlsson 2016), lipid modifications and a reorganization of lipid bilayers (Anitei, Stange et al. 2017) or steric repulsion of coat and adaptor proteins due to their crowding (Busch, Houser et al. 2015, Derganc and Copic 2016). Although the possibility of these mechanisms have been demonstrated *in vitro*, their importance *in vivo* remain unknown (detailed in Material and Methods) (Boettner, D'Agostino et al. 2009, Carlsson and Bayly 2014, Kukulski, Picco et al. 2016).

We investigated an alternative potential mechanism of CME in a yeast cell mutant model in which turgor pressure is relieved and actin polymerization is specifically inhibited (Fig. 1a, Fig. S1-2). This potential mechanism was suggested to us by the observation that there is a common

2

74   amino acid sequence pattern called prion-like domains (PLD) found among coat and adapter
75   proteins (Fig. 1a) (Alberti, Halfmann et al. 2009, Malinovska, Kroschwald et al. 2013). Such
76   proteins are known to phase separate *in vitro* and in cells. Phase separation leads to spherical
77   condensates or droplets that are hundreds of nanometers to micrometers in size with a range of
78   viscoelastic properties (Guilak, Tedrow et al. 2000, Pappu, Wang et al. 2008, Brangwynne,
79   Eckmann et al. 2009, Hyman, Weber et al. 2014, Banjade, Wu et al. 2015, Jiang, Wang et al.
80   2015, Kroschwald, Maharana et al. 2015, Molliex, Temirov et al. 2015, Nott, Petsalaki et al.
81   2015, Zhang, Elbaum-Garfinkle et al. 2015). The idea that membranes can be deformed by
82   liquid-liquid phase separation of droplets is supported by *in vitro* evidence of membrane
83   nanotubes formed by displacement of small polymer droplets contained within giant
84   phospholipid bilayer membrane vesicles (Li, Lipowsky et al. 2011). We postulate that such
85   droplets exist at CME initiation sites and that, owing to their viscoelastic properties and
86   interfacial tension, bind to the plasma membrane adaptors and generate a force that drives
87   invagination of the membrane (Hertz 1882, Johnson 1971, Style, Hyland et al. 2013).
88
89   **PLD-containing CME proteins accumulate and phase separate at cortical sites**
90
91   Evidence that a protein droplet (henceforth called the cortical droplet) could form at CME sites
92   include first, electron and light microscopic studies that reveal a region surrounding CME
93   membrane invaginations and mature vesicles of ~200 nm diameter that are devoid of ribosomes
94   (Kukulski, Schorb et al. 2012, Picco, Mund et al. 2015). This "exclusion zone" thus appears to
95   present a physical barrier to large molecular complexes at least as large as ribosomes (> 10 nm)
96   (Kukulski, Schorb et al. 2012). Furthermore, we and others have observed an object at cortical
97   sites of ~200 nm diameter by super-resolution imaging of the endocytic coat protein Sla1 in cells
98   treated with Latrunculin A (Lat A), an inhibitor of actin polymerization. Therefore, the exclusion
99   zone cannot be attributed to F-actin bundles (Fig. 1b, Fig. S3) (Picco, Mund et al. 2015). Our
100   results agree with quantitative immuno-EM data which show that many endocytic coat proteins
101   (including Sla1/2 and Ent1/2) are located in a space of similar dimensions, consistent with a
102   protein droplet that associates with the membrane on cortical sites (Idrissi, Grotsch et al. 2008,
103   Idrissi, Blasco et al. 2012).

3
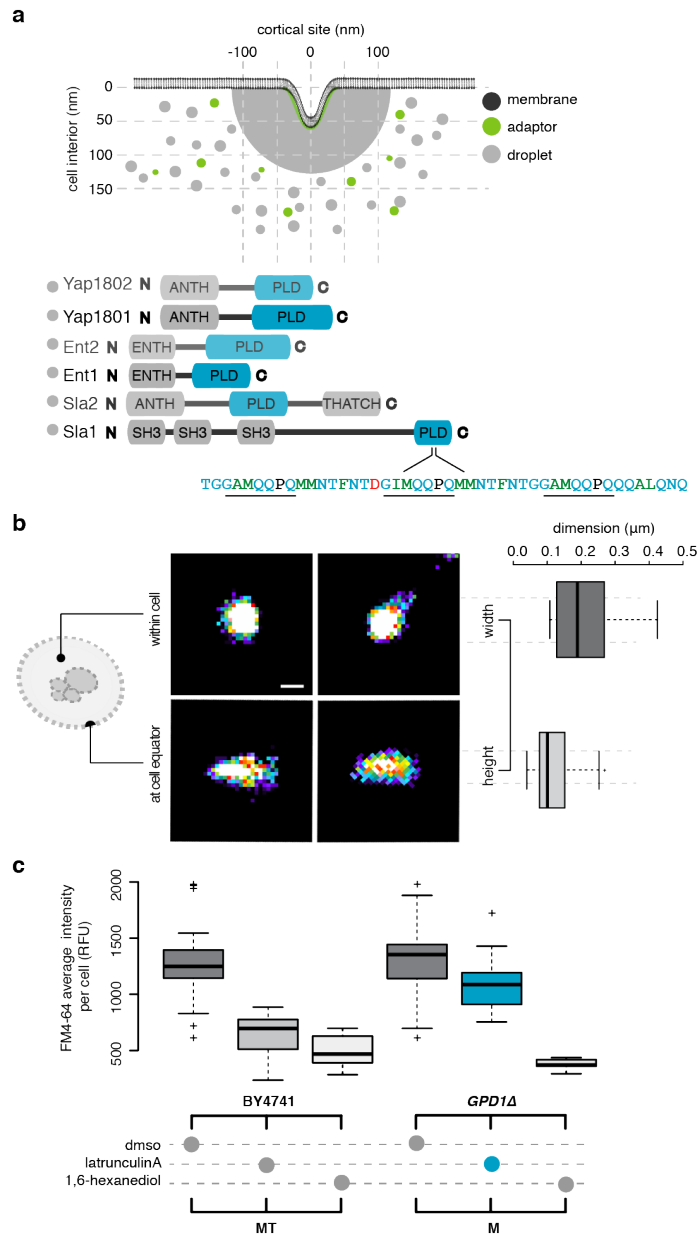
Figure 1 | Assembly of proteins into a cortical droplet drives clathrin-mediated endocytosis (a) (Upper panel) Illustration of the geometry of a plasma membrane (dark grey) invagination into the cell during clathrin-mediated endocytosis (CME). 70 nm invagination is required for vesicle scission to occur. Electron microscopic data suggest that clathrin-coated plasma membrane patches are surrounded by a cortical body of ~200 nm diameter (light grey) before appearance of actin structures. Clathrin heavy and light chains (Chc1 and Clc1) interact with adaptor proteins (Ede1 and Syp1) to form a lattice on the membrane (in green). Subsequently, early coat proteins (light grey), such as Sla1/2, Ent1/2, and Yap1801/2, directly bind to the adaptor-clathrin lattice and form the cortical body (in grey). (lower panel) Coat proteins contain "Prion-like domains" (PLD, in blue) that include tandem repeats of asparagine and glutamine. (b) Geometry and size distribution of coat protein Sla1-GFP at cortical sites measured using super-resolution microscopy (dSTORM). Lateral x, y resolution was ~10 nm. Pseudo-color reconstructed

4

117   images show circular structures (left panels) when viewed from the top, or within cells (left, upper), but
118   form narrow ellipses when imaged at the equator of cells (left, lower). Automatic segmentation and
119   morphological analysis (right) were performed on these reconstructed images to determine the width (209
120   ± 10 nm) and height (118 ± 6 nm) of cortical bodies (mean ± sd; n = 250), consistent with other electron
121   and light micrographic evidence. (c) Lipophilic cargo membrane-labelling dye FM4-64 is taken up into
122   vesicles by CME in wild type BY4741 (left) and *GPD1Δ* cells (eliminates turgor pressure; right) treated
123   with either DMSO, latrunculin A (prevents F-actin polymerization) or 1,6-hexanediol (disrupts liquid-
124   liquid phase separated protein droplets). Each boxplot (center line, median; box, upper and lower
125   quartiles; whiskers, 1.5x IQR; crosses, outliers) shows the relative fluorescence units of n = 50 cells. Note
126   that *GPD1Δ* cells can undergo CME in the absence of F-actin polymerization (blue) because there is no
127   turgor pressure in these cells (Fig. S1-2).
128
129   The simple alcohol 1,6-hexanediol (HD) has been demonstrated to prevent liquid-liquid phase
130   separation of proteins *in vivo* and *in vitro* (Updike, Hachey et al. 2011, Kroschwald, Maharana et
131   al. 2015, Molliex, Temirov et al. 2015, Wheeler, Matheny et al. 2016). CME, as measured by
132   cell uptake of a lipophilic membrane-bound fluorescent dye (FM4-64), was inhibited by HD,
133   whether or not turgor pressure and actin polymerization were present (Fig. 1c, left *versus* right
134   panels, respectively). Furthermore, an HD dose-response of uptake of the fluorescent dye
135   (Lucifer Yellow) into vacuoles and formation of puncta monitored as Sla1-GFP fluorescence at
136   cortical sites were prevented, but not in cells treated with the related alcohol 1,2,3-hexanetriol
137   that does not disrupt droplets (Fig. 2a, Fig. S4). The other PLD-containing proteins, including
138   Sla2, Ent1, Ent2, Yap1801 and Yap1802, all failed to form puncta in cells treated with HD (Fig.
139   S4). Pulse-chase experiments showed that HD-dependent dissolution of Sla1 puncta was
140   reversible (Fig. S5 and Movie S1). Finally, PLD-containing proteins can also form amyloid
141   aggregates, which can be diagnosed by binding and co-localization of Thioflavin T (ThT) to the
142   aggregates (Khurana, Coleman et al. 2005). We observed no colocalization of ThT with Sla1-
143   mCherry-labelled puncta (Fig. S6).
144
145   The PLDs of cortical CME proteins were essential to their localization to cortical sites (Fig. 2b).
146   Furthermore, CME was significantly reduced in cells where the PLDs of Sla1 and Ent1 were
147   deleted and with substitutions of proline for other residues in the Sla1 PLD, which weakens the
148   driving force for phase separation (Fig. 2c, Fig. S7) (Toombs, McCarty et al. 2009, Crick, Ruff et
149   al. 2013). Our results support evidence that there is a functional redundancy among most of the
150   PLD-containing proteins with the two that are more essential, perhaps required for specific
151   functions mediated by other domains within their sequences (Watson, Cope et al. 2001).
152

153
154
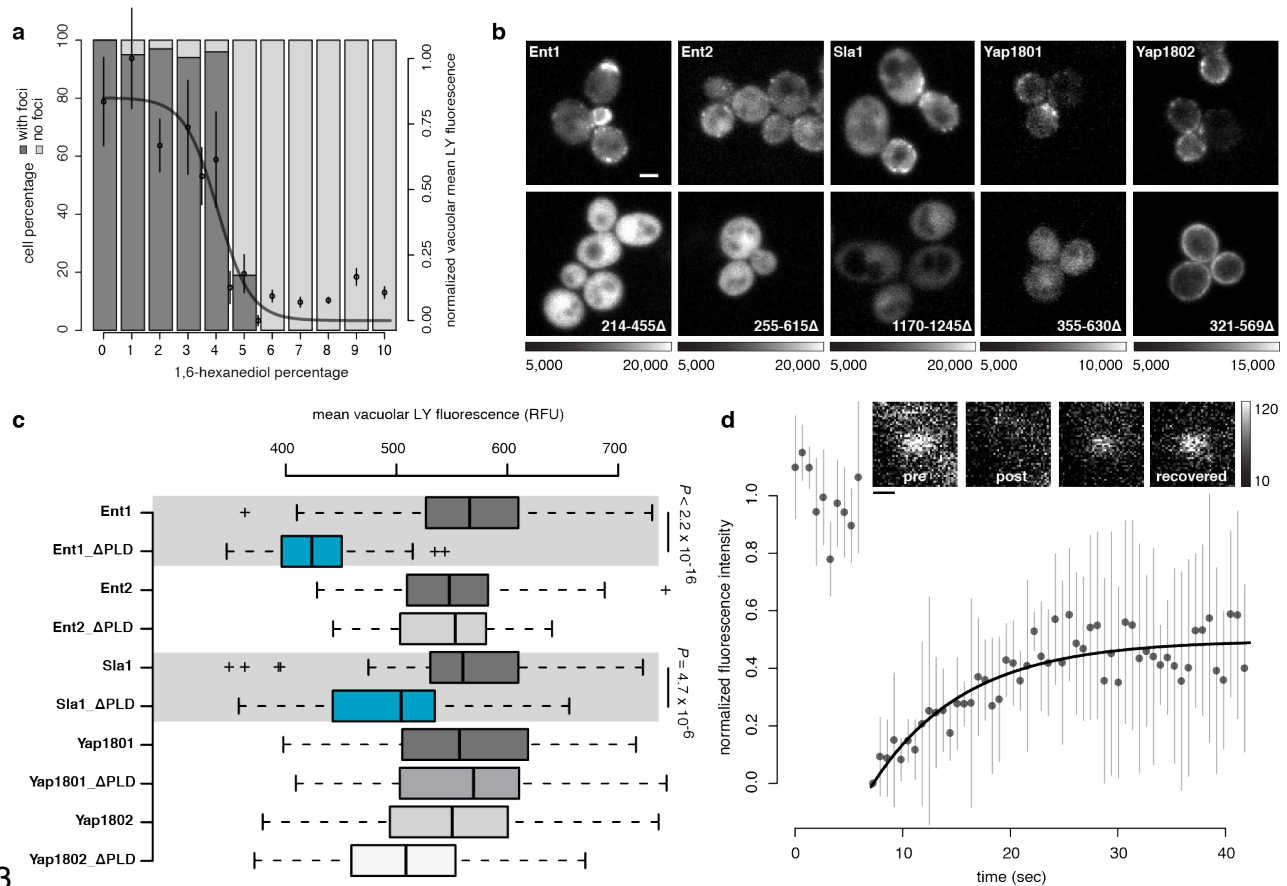
Figure 2 | CME adaptor and coat proteins phase separate to form droplets (a) 1,6-hexanediol (HD), disrupts cortical droplets in an all-or-none manner. Barplot shows percentage of cells that contain Sla1-GFP foci (dark grey), or not (light grey), as a function of HD concentration monitored by counting fluorescent puncta containing Sla1-GFP at cortical sites 5 minutes after HD treatment (n = 150 cells). Plot overlay (in black) shows quantification of lucifer yellow fluorescent dye uptake in CME vesicles (mean ± sd; n = 25 foci; logistic fit) (b) Prion-like domains (PLDs) are essential for localization of proteins to the cortical sites. Fluorescence images of cortical localization of Ent1, Ent2, Sla1, Yap1801 and Yap1802 fused to Venus YFP. Localization of full-length (upper panels) *versus* C-terminal PLD truncation mutants of the proteins (lower panels). Amino acid positions of the deleted PLDs are indicated for respective images. Grayscale dynamic range for image pairs are indicated below. Scale bar, 2 μm. (c) Quantification (box center line, median; box limits, upper and lower quartiles; whiskers, 1.5x IQR; crosses, outliers) by fluorescence microscopy of lucifer yellow dye uptake for strains that express either full-length or PLD-truncated Ent1, Ent2, Yap1801, Yap1802 and Sla1 (as detailed in panel b). We observed a significant decrease in CME for PLD truncation mutants of Sla1 and Ent1 (n = 100 cells; two-sided t-test; see Material and Methods). (d) Coat proteins exchange with cortical droplets at rates typical of those observed for proteins that compose other protein droplets. Fluorescence recovery after photo bleaching (FRAP) of Sla2-GFP, GFP signal recovery was measured within a segmented Sla1-mCherry region of interest to ensure that FRAP was acquired within the cortical droplet (mean ± sd; n = 10 cells. Data was fitted to a single term recovery equation (full line) (Material and Methods). Incomplete fluorescence recovery suggests that cortical droplets are viscoelastic. Representative foci images before bleaching,

6

175 upon bleaching, and after recovery are shown in inserts. 8-bit grayscale values, 10 to 120. Scale bar, 250
176 nm.
177
178 The interactions among proteins in liquid-liquid phase separated droplets are expected to be
179 weak and this is assessed by their rapid exchange within and between droplets and their
180 surroundings (Brangwynne, Eckmann et al. 2009, Elbaum-Garfinkle, Kim et al. 2015, Lin,
181 Protter et al. 2015, Feric, Vaidya et al. 2016). In fluorescence recovery after photobleaching
182 (FRAP) experiments we measured equivalent mobile and immobile fractions (0.50 ± 0.02; mean
183 $\pm$ sem) for the protein Sla2 and a rapid recovery time (5.96 ± 1.15 seconds; mean $\pm$ sem) (Fig.
184 2d), similar to other protein and nucleic acid droplets including the dense internal fibrillar
185 component of *X. laevis* nucleoli (Feric, Vaidya et al. 2016). Taken together, these results support
186 the hypothesis that the cortical bodies are phase separated viscoelastic droplets. We next set out
187 to determine the material properties of the cortical droplets and to test our postulate that their
188 binding to the plasma membrane generates the force that drives invagination of the membrane.
189
190 **Cortical droplets can mechanically deform both cytosol and membrane**
191
192 We hypothesized that free energy released by cortical droplet phase separation is converted into
193 mechanical work to deform the membrane and the cytosol. This mechanical work is manifested
194 as an inward pressure on the membrane created by expansion of the droplet and the requirement
195 that volume of the droplet is conserved. Phenomena where geometric organization of matter is
196 driven by the balances of opposing forces have been described at subatomic up to stellar scales,
197 examples of which include "fingering instabilities" (Kull 1991, Hester 2008, Xi, Byrnes et al.
198 2017).
199
200 The mechanics of CME can be described by analogy to a soft viscoelastic and sticky balloon
201 bound to a soft elastic sheet (Fig. 4a, Movie S2). If you stuck your finger through the center of
202 the sheet-balloon interface to create an invagination, the surface area of the balloon would have
203 to increase to maintain the volume and density of the balloon constant. Equally, but in an inverse
204 sense, if you were to grasp the sticky surface of the balloon with your hands and pull outwards
205 equally over the surface, except at the elastic sheet-balloon interface, a tiny increase of the
206 surface area would require a compensating adjustment of the shape so that the balloon keeps a
207 constant volume. Since force is being applied outwards everywhere except at the sheet balloon
208 interface, it is here that an invagination of the membrane-balloon interface would compensate for
209 the pressure generated by the outward force on the balloon surface.
210
211 In the case of CME, the grasping force is caused by binding of molecules at the cortical droplet-
212 cytoplasm interface. Balance between this binding and elastic deformation energies is achieved
213 when the membrane invaginates. This idea is captured in a simple phenomenological model
214 expressed as the sum of mechanical strain energy (ϕ term) and work (ψ term), respectively;
215

7

216
$$U \sim \phi \cdot \delta^{1+\varepsilon} - \psi \cdot \delta \; ; \tag{1}$$

217

218 Here, U is the mean-field energy, δ is the invagination depth of both the membrane and cytosol
219 (which are coupled to each other by virtue of conservation of volume of the droplet) and the
220 exponent $\varepsilon > 0$ reflects the deformation geometry (Material and Methods). Close to equilibrium
221 (as $\partial U/\partial \delta$ approaches 0) we expect invagination to balance the two contributions so that δ^*
222 minimizes energy in (1) resulting in,

223

224
$$\delta^* = \left(\frac{\psi}{\phi \, (1 + \varepsilon)} \right)^{\frac{1}{\varepsilon}} \; ; \tag{2}$$

225

226 Equation (2) shows that the invagination depth δ is determined by the ratio ψ/φ and the
227 deformation geometry ε. Values of φ and ψ can be determined as functions of individual
228 geometries, elasticities, and viscosities of cytosol, droplet and membrane and interfacial tensions
229 among them (Material and Methods). These in turn can be determined by super-resolution
230 imaging (geometries) and elastic and viscous moduli, taken from the literature or determined by
231 active micro-rheology experiments as described next.

232

233 We used active rheology to determine the material properties of the cytosol in which cortical
234 droplets are embedded and then, because the droplets are too small to probe directly, we
235 calculated their properties through well-understood relationships between the properties of
236 materials in contact and their resulting geometries, as described below. Specifically, we used
237 optical tweezers to examine the frequency-dependent amplitude and phase responses of
238 polystyrene beads that are embedded in cells (Fig. 3a, Material and Methods). 200 nm diameter
239 polystyrene beads were integrated into cells by osmoporation (Fig. S8) (da Silva Pedrini, Dupont
240 et al. 2014). Measurements of passive diffusion of the beads showed mean square displacements
241 (MSD) close to that of random mechanical noise caused by vibration of the microscope (Fig.
242 S8). Furthermore, we established that the osmoporation procedure did not affect rheological
243 properties of cells by measuring the MSD of expressed viral capsid microNS particles labeled
244 with GFP in untreated or osmoporated cells and showing that their diffusion behaviors were
245 identical (Fig. S9) (Munder, Midtvedt et al. 2016).

246

247 For active rheology experiments, we used an acousto-optic device to oscillate the position of the
248 optical trap in the specimen plane at frequencies over four orders of magnitude and measured the
249 displacement of trapped beads from the trap center using back focal plane interferometry (Fig.
250 3b). We could thus measure the viscoelastic properties of the cytosol surrounding the beads by
251 measuring their phase and amplitude response to the oscillations of the optical tweezers. Then by
252 calculating the power spectrum of unforced fluctuations of the bead we obtained storage (G′) and

253   loss (G″) moduli as a function of frequency (Fig. 3c-d, Fig. S10, Material and Methods) (Fischer,
254   Richardson et al. 2010, Hendricks and Goldman 2017).
255
256   In addition to obtaining quantities essential to calculate material properties of the cytoplasm and
257   droplet, active rheology combined with spatiotemporal dynamics of interacting materials can
258   inform of their structures. The mechanical properties of living cells can be compared to that of
259   the popular children's toy "Silly Putty" (Cross 2012). Like this material, cells and underlying
260   structures show different mechanical properties depending on the rates at which forces are
261   applied to them (Hendricks, Holzbaur et al. 2012, Guo, Ehrlicher et al. 2013, Guo, Ehrlicher et
262   al. 2014). If a force is applied at a low velocity, the cell behaves like a viscous fluid; flowing and
263   taking on whatever shape it is forced into. When a force is applied at higher velocity, however,
264   the material behaves like an elastic object, bouncing back to its original shape. As we discuss
265   below, these behaviors reflect the manner and strengths with which the molecules that make up a
266   material interact with each other and their environment.
267
268   In specific terms, the material properties of the yeast cytoplasm and its interactions with the
269   cortical droplet could be interpreted from the complex modulus versus frequency plot as follows
270   (Fig. 3d). The inflection of the G' modulus at 2 Hz results in similar G' and G" values at low
271   frequencies, which indicates that the cytosol is more viscous near rest. When deformed by the
272   droplet growth (at a velocity of growth = 2360 ± 120 nm s^{-1}; corresponding to a stress at ~30 ± 2
273   Hz) the cytosol is more elastic, whereas membrane invagination occurs at a rate at which the
274   cytoplasm is more viscous (a velocity of 7.4 ± 2.5 nm s^{-1}; corresponding to 0.1 ± 0.04 Hz) (Fig.
275   1b, 3d, Fig. S11). The G′ and G″ we measured are similar to the cytoplasm of adherent
276   mammalian cells and indicate that the beads are confined within a dense network of interacting
277   molecules (Hendricks, Holzbaur et al. 2012, Guo, Ehrlicher et al. 2013, Guo, Ehrlicher et al.
278   2014).
279

9
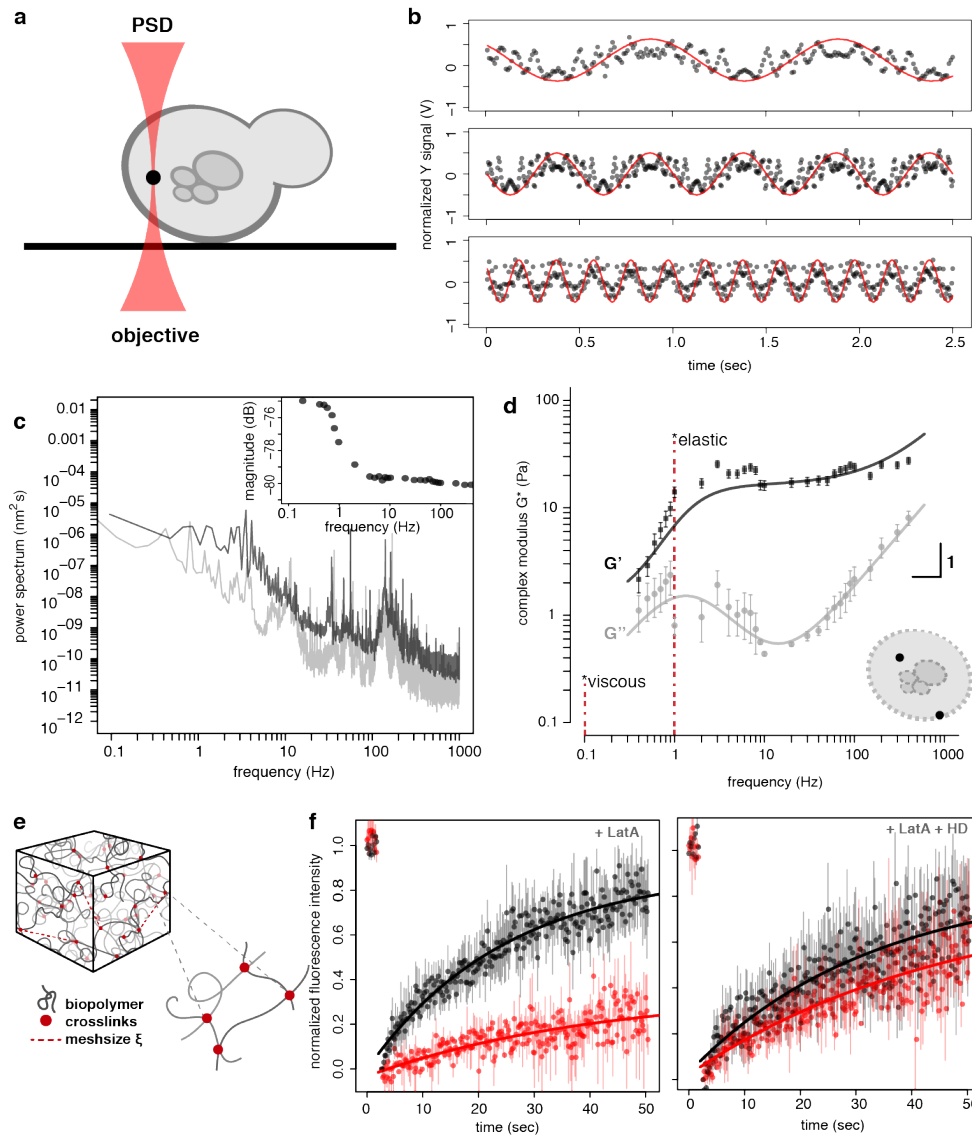
280
281
282 **Figure 3 | Cytosol and cortical droplets are composed of a viscoelastic amorphous network of**
283 **interacting proteins** (a) We used optical tweezers (red beam between the microscope objective and a
284 position sensitive detector (PSD) coupled to an acousto-optic device (AOD) to oscillate polystyrene beads
285 in cells. Two pulses of osmotic shock were used to osmoporate 200 nm polystyrene beads (black) into Lat
286 A-treated haploid yeast *GPD1Δ* cells. (b) PSD output signal in volts (V) as a function of time for
287 acquisitions made at 1Hz (top), 2 Hz (middle) and 5 Hz (bottom). A bead, located in the cell periphery,
288 was oscillated with the AOD in the Y-axis of the specimen plane with fixed tweezer movement amplitude
289 (normalized red curve) at different frequencies. The recorded PSD raw traces (black points) were also
290 normalized to a corresponding magnitude range (coherence cutoff of 0.9). (c) Power spectrum of the
291 oscillated bead (black) with magnitude of response as a function of frequency (insert). (d) Decomposition
292 of G* as a function of frequency into G′ (storage modulus; darker squares) and G″ (loss modulus; light
293 shade circles) for beads distributed at both the cell periphery and interior (see schematic insert; mean ±
294 sd; n = 17 cells) with an average trap stiffness k_{trap} (mean ± se; 8.0 x 10^{-5} ± 2.7 x 10^{-5} N m^{-1}) and

10

295   photodiode sensitivity factor β (mean ± se; 10.7 x 10^3 ± 2.3 x 10^3 nm V^{-1}). Data was fitted to a model of
296   an entangled and crosslinked network of flexible polymers (Material and Methods; Eq. 2.9-2.10). Dashed
297   lines indicate frequency range for more viscous or more elastic behavior. (e) 3D illustration and zoom-in
298   of the latticework composed of amorphous protein chains (grey filaments) with the binding sites (red
299   dots) through which they are non-covalently associate and the mesh size (dashed red line). (f)
300   Fluorescence recovery after photo bleaching (FRAP) of fluorescent dye (FITC)-conjugated dextran of
301   10.4 nm within a Syp1-mCherry focus (red) or neighbouring cytosolic regions without Syp1 signal
302   (black) in either Lat A-treated (left panel) or Lat A and HD-treated *GPD1Δ* Syp1-mCherry cells (right
303   panel). Data points represent mean normalized fluorescence recovery (mean ± SEM; n = 10 cells). Values
304   for distinct dextran-FITC sizes and cell region were fitted to a single term recovery equation (Material
305   and Methods).
306
307   We could now determine the mechanical properties of the cortical droplet as follows. First, our
308   data are consistent with both cortical droplets and cytosol behaving as predominantly elastic
309   materials (Fig. 3d). Classic Hertz theory relates contact geometries of elastic materials to their
310   mechanical properties. We could thus, use the geometry of the cortical droplets determined in
311   our super-resolution imaging experiments, and the moduli of the cytosol in which they are
312   embedded to estimate the cortical droplet elastic modulus to be 59 Pa (Fig. 1b, 3d, Material and
313   Methods; Eq. 3.7-3.10) (Hertz 1882). These results are consistent with protein condensates that
314   form elastic materials (Reichheld, Muiznieks et al. 2017) and suggest that the cortical droplets
315   have similar material properties as the surrounding cytosol, which has an elastic (or Young's)
316   modulus of 45 Pa at 1 Hz (Material and Methods). We estimated the average mesh size and
317   permeability of the cortical droplets by probing them with fluorophore-conjugated dextran
318   molecules of 2.4, 5.8, and 10.4 nm in size. We measured FRAP and colocalization of thes
319   dextran molecules with either Sla1-mCherry or Syp1-mCherry puncta (Fig. 3e-f, Fig. S12-13).
320   Both 2.4 nm and 5.8 nm dextran-FITC recovered equally in the droplet and cytosolic zones. In
321   contrast, the 10.4 nm dextran-FITC molecules scarcely permeate the PLD-rich protein network
322   in the droplet whereas they are mobile in the neighbour cytosol. If cortical droplets are dissolved
323   by addition of 1,6-hexanediol, we observe equivalent mobility of 10.4 nm dextran-FITC between
324   cortical sites, labelled with the protein Syp1-mCherry, which is membrane-bound at cortical
325   patches in an HD-resistant manner, and neighboring cytosol (Fig. 3f, Fig. S13). These results are
326   consistent with an exclusion zone for ribosomes as discussed above and with exclusion of
327   dextrans by known protein-RNA phase separated droplets called P granules (Updike, Hachey et
328   al. 2011, Kukulski, Schorb et al. 2012, Wei, Elbaum-Garfinkle et al. 2017).
329
330   **Cortical droplet binding to cytosol provides the energy to drive membrane invagination**
331
332   The deformation of the membrane in response to contact with a soft object depends on the
333   geometries and mechanical properties of the object and the vessel it is in (in our case the cytosol
334   of a cell) and the membrane (Fig. 4a). Evidence from electron and super-resolution fluorescence
335   microscopy indicate that the favored geometry of the membrane is flat with invagination

336 centered in the middle of the droplet (Fig. 4a, lower). Such geometries could be explained by a
337 local radial stress-gradient generated by the droplet adhesion to both the membrane and cytosol,
338 or by local binding of adaptor proteins and distinct lipid composition. Simply stated, as the
339 droplet grows the binding to the cytosol draws it inward and the membrane follows, mediated by
340 its own binding to the droplet and the requirement that the volume of the droplet be conserved.
341
342 We could now quantify the work performed by the droplet to invaginate the membrane using the
343 storage and loss moduli obtained from the micro-rheology experiments, geometric data obtained
344 from super-resolution imaging and other data available from the literature, to solve the explicit
345 form of the ϕ and ψ terms (mechanical strain and work, respectively) in Equation (1) as
346 functions of membrane and cytosol invagination δ (Material and Methods; Eq. 4.25-4.26). Using
347 the Young-Laplace equation, we first estimated an interfacial tension for the droplet-cytosol
348 interface to be approximately γ_{dc} of 7×10^{-5} N•m^{-1}. This estimate is based on the pressure
349 difference across the cytosolic interface and the droplet mean curvature (Material and Methods;
350 Eq. 4.6). Our estimate for the interfacial tension falls within the range of 10^{-5} N•m^{-1} to 10^{-4} N•m^{-1}
351 that has been reported for other protein droplets, including nucleoli and P granules (Material and
352 Methods; Eq. 4.9) (Brangwynne, Mitchison et al. 2011, Elbaum-Garfinkle, Kim et al. 2015).
353
354 Given our estimates of γ_{dc} we also determined the work of adhesion that is released when the
355 droplet surfaces are created, as described by the Young-Dupré equation (Fig. 4a, Material and
356 Methods; Eq. 4.11). We calculated an adhesion energy (ψ) of 4.9×10^{-18} J from interactions
357 between the cortical droplet and both the membrane and cytosol (Fig. 4b, Fig. S14, Material and
358 Methods; Eq. 4.26). Our results suggest that the most significant contribution of the mechanical
359 energy comes from the droplet-cytosol interface, where the adhesion energy of 2.9×10^{-18} J is
360 enough to overcome an energy penalty of 2.4×10^{-18} J to deform the membrane and the cytosol.
361 This energy cost includes the elastic, viscous, and interfacial stress penalties (Fig. 4b, Fig. S14,
362 Table S4). We also calculated an average adhesion energy of 1.3 kJ•mol^{-1} at the droplet-cytosol
363 interface (Material and Methods), which is consistent with the free energies expected of non-
364 covalent interactions (Mahadevi and Sastry 2016).
365
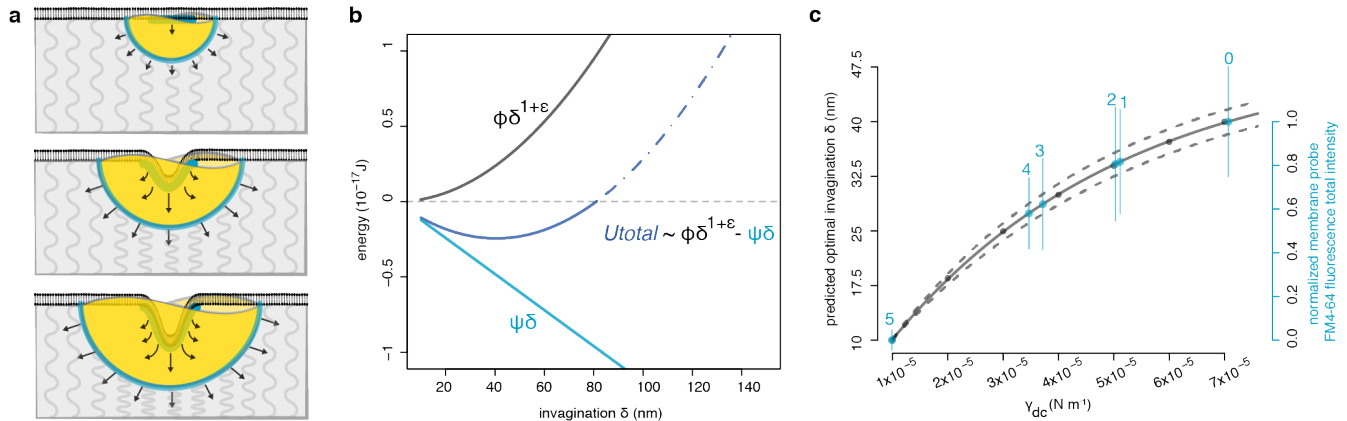
Figure 4 | Cortical droplets do mechanical work to deform the membrane and cytosol (a) Illustration of a cortical droplet (gold) that binds to (wets) a bilayer membrane (black) and drives membrane invagination (top to bottom). Resultant membrane deformations reflect how forces balance under a Young-Dupré adhesion gradient (blue lines and arrows). Resistance to deformation is represented by grey curved lines. (b) Equation (1) (insert) was used to calculate the energy penalties (ϕ) and contributions (ψ) at the cytosol and membrane interfaces with the cortical droplet. Total energy of the system (dark blue), energy penalties (black) and energy contributions (light blue) are presented as a function of membrane invagination (δ). The energy of membrane invagination is favourable for δ between about 15-80 nm (solid blue line) and unfavourable above 80 nm (dashed blue line). Quantities used to calculate energies are detailed in Figure S14 and Tables S3-4. (c) Our model predicts that vesicle size is proportional to the strength of droplet intermolecular protein-protein interactions that are proportional to γ_{dc}, the droplet-to-cytosol interfacial tension. Predicted membrane invagination δ as a function of γ_{dc} (left axis and black points). Data points were fitted to an exponential decay function (full line) with 95% confidence interval (dashed lines). Titration of 1,6-hexanediol was used to reduce intermolecular cohesion and therefore γ_{dc} resulting in reduced vesicle size as measured by uptake of the lipophilic membrane probe FM4-64 into *GPD1Δ* Sla1-YFP cells treated with Lat A (Right axis, red) *versus* % HD (blue numbers, n= 25, mean ± sd) expressed as a function of the droplet-cytosol interfacial tension γ_{dc} (Material and Methods).

Our model provides a physical framework to explain how cortical droplets do the mechanical work needed to induce invagination of membranes in actin-independent CME. The interface between droplets, formed, by phase separation of disordered proteins into cortical bodies, and the cytosol- membrane interface deforms the surrounding materials through adhesive interactions. Invagination occurs when ψ dominates ϕ and this is favored within the observed δ interval of 40 nm to 80 nm (Fig. S14). Notably, this predicted δ interval is within the range of plasma membrane invagination of ~70 nm at which point a membrane scission mechanism is activated and vesicle generation is completed (Idrissi, Blasco et al. 2012).

We propose that cortical droplets store and dissipate mechanical energy in the form of surface tension, whereby the composition of the droplets determines their interfacial interactions and provides the energy for adhesion and invagination of membranes. Accordingly, the underlying

13

398   energy stored within the droplets and the balance of interactions amongst droplet components
399   and solvent governs the nature of the interface. The effective potential energy ψ of droplets,
400   which is equivalent to the total work of adhesion, should be dictated by the density and strengths
401   of physical interactions amongst proteins within the droplet (the droplet cohesion and interfacial
402   tensions). We tested this hypothesis by weakening the favorable free energies of the protein-
403   protein interactions that hold droplet components together using 1,6-hexanediol (HD). These are
404   the interactions that drive the phase separation of cortical droplets, and so would correspond to a
405   decrease of the droplet surface tension (γ_{dc} or ψ). Our model predicts that invagination depth
406   should continuously vary with ψ from Equation (2). We titrated HD below the effective
407   concentration that prevents protein phase separation and quantified individual membrane
408   excision events by quantifying uptake of the lipophilic membrane probe FM4-64 into cells by
409   fluorescence microscopy (Fig. 2a, Material and Methods). In Lat A treated *GPD1Δ* cells, this
410   measures the amount of labeled membrane taken up into cells under the action of cortical
411   droplets alone. By increasing subcritical HD concentration (corresponding to a decrease in ψ),
412   the average fluorescence-labeled membrane per vesicle (a proxy for invagination δ) was
413   continuously reduced over one order of magnitude in the value of γ_{dc} (Fig. 4c, Material and
414   Methods; Eq. 2.8). This observation fits with the reduced membrane invagination that we
415   predicted at the outset (*i.e.*, that δ scales with the ψ/ϕ ratio) when the droplet cohesion (γ_{dc} or ψ)
416   is also reduced (Fig. 4c, Material and Methods; Eq. 4.2).

417

418   **Discussion**

419

420   Our results provide a framework for answering many questions regarding CME and other
421   membrane budding processes. Given our observations, how is CME coupled to multiple
422   signaling pathways that integrate to regulate vesicle formation? For instance, the PLD-containing
423   CME proteins we investigated are enriched for multiple phosphorylation sites, which undergo
424   changes in response to activation of a CME-regulating signaling pathway (Kanshin, Bergeron-
425   Sandoval et al. 2015). Since the amount and distribution of charge in disordered regions of
426   proteins regulate their interactions and conformations (Das and Pappu 2013), such post-
427   translational modifications may be important to regulating CME. Our fluorescence microscopy
428   and electron micrographic evidence from the literature suggests that the cortical droplet remains
429   associated temporarily with mature vesicles (Kukulski, Schorb et al. 2012). Does the droplet play
430   any role in trafficking and fusing with, for instance, plasma membrane (protein recycling) or
431   lysosome (protein degradation)? CME underlies several fundamental mechanisms of vesicle
432   trafficking and attendant membrane and vesicle protein cargo transport, including late secretory
433   pathways, endocytosis and neuronal synaptic vesicle recycling. Yeast and human proteins
434   implicated in clathrin-mediated vesicle trafficking are enriched for long disordered protein
435   domains (47/23% of proteins with long consecutive disordered regions of 30 residues and more
436   for humans and yeast, respectively) whereas those involved in two other vesicle trafficking
437   systems are not (COPI: 8/5%; COPII: 8/5%) (Pietrosemoli, Pancsa et al. 2013). These

438   observations argue for investigating the generality and conservation of protein droplet adhesion-
439   driven membrane invagination as the basis of clathrin-mediated vesicle trafficking in the absence
440   of actin polymerization.
441

442   It is possible that other liquid-liquid phase separated protein and protein nucleic acid droplets
443   may influence cellular sub-structural dynamics and thus contribute to shaping cell, tissue, and
444   organism morphology (Bergeron-Sandoval, Safaee et al. 2016, Bauerlein, Saha et al. 2017).
445   More broadly, interfacial contact potentials between different biological materials could
446   represent a vastly underestimated source of complex pattern formation in biology, such as has
447   been observed in embryonic tissue layers (Foty, Pfleger et al. 1996) or recently in a model of
448   growing brain convolutions (Tallinen, Chung et al. 2016), in protein stabilization (Gupta, Donlan
449   et al. 2017) and in the ability of clathrin-coated structures to wrap around and pinch collagen
450   fibers (Elkhatib, Bresteau et al. 2017).
451

Acknowledgments

453

461

Author contributions

463

464   L.P.S.B. and S.W.M. designed all of the research and R.V.P. helped in research designing;
465   L.P.S.B. performed biological research; L.P.S.B. and H.K.H. performed micro rheology
466   experiments; L.P.B.S., H.K.H., A.J.E. and A.G.H analyzed micro rheology data; L.P.S.B., A.J.E.
467   and S.W.M. analyzed biological data; L.P.B.S., H.K.H. and P.F. developed physical droplet
468   model; L.P.S.B., R.V.P., and S.W.M. combined physical models with data analysis; all authors
469   wrote the paper.

470

Supplementary Materials

472   Materials and Methods
473   Figures S1-S14
474   Tables S1-S4
475   Movies S1-S2

References

1. Aghamohammadzadeh, S. and K. R. Ayscough (2009). "Differential requirements for actin during yeast and mammalian endocytosis." Nat Cell Biol **11**(8): 1039-1042.

2. Alberti, S., R. Halfmann, O. King, A. Kapila and S. Lindquist (2009). "A systematic survey identifies prions and illuminates sequence features of prionogenic proteins." Cell **137**(1): 146-158.

3. Anitei, M., C. Stange, C. Czupalla, C. Niehage, K. Schuhmann, P. Sala, A. Czogalla, T. Pursche, U. Coskun, A. Shevchenko and B. Hoflack (2017). "Spatiotemporal Control of Lipid Conversion, Actin-Based Mechanical Forces, and Curvature Sensors during Clathrin/AP-1-Coated Vesicle Biogenesis." Cell Rep **20**(9): 2087-2099.

4. Avinoam, O., M. Schorb, C. J. Beese, J. A. Briggs and M. Kaksonen (2015). "ENDOCYTOSIS. Endocytic sites mature by continuous bending and remodeling of the clathrin coat." Science **348**(6241): 1369-1372.

5. Banjade, S., Q. Wu, A. Mittal, W. B. Peeples, R. V. Pappu and M. K. Rosen (2015). "Conserved interdomain linker promotes phase separation of the multivalent adaptor protein Nck." Proc Natl Acad Sci U S A **112**(47): E6426-6435.

6. Bauerlein, F. J. B., I. Saha, A. Mishra, M. Kalemanov, A. Martinez-Sanchez, R. Klein, I. Dudanova, M. S. Hipp, F. U. Hartl, W. Baumeister and R. Fernandez-Busnadiego (2017). "In Situ Architecture and Cellular Interactions of PolyQ Inclusions." Cell **171**(1): 179-187 e110.

7. Bergeron-Sandoval, L. P., N. Safaee and S. W. Michnick (2016). "Mechanisms and Consequences of Macromolecular Phase Separation." Cell **165**(5): 1067-1079.

8. Boettner, D. R., J. L. D'Agostino, O. T. Torres, K. Daugherty-Clarke, A. Uygur, A. Reider, B. Wendland, S. K. Lemmon and B. L. Goode (2009). "The F-BAR protein Syp1 negatively regulates WASp-Arp2/3 complex activity during endocytic patch formation." Curr Biol **19**(23): 1979-1987.

9. Brangwynne, C. P., C. R. Eckmann, D. S. Courson, A. Rybarska, C. Hoege, J. Gharakhani, F. Julicher and A. A. Hyman (2009). "Germline P granules are liquid droplets that localize by controlled dissolution/condensation." Science **324**(5935): 1729-1732.

10. Brangwynne, C. P., T. J. Mitchison and A. A. Hyman (2011). "Active liquid-like behavior of nucleoli determines their size and shape in Xenopus laevis oocytes." Proc Natl Acad Sci U S A **108**(11): 4334-4339.

11. Busch, D. J., J. R. Houser, C. C. Hayden, M. B. Sherman, E. M. Lafer and J. C. Stachowiak (2015). "Intrinsically disordered proteins drive membrane curvature." Nat Commun **6**: 7875.

12. Carlsson, A. E. and P. V. Bayly (2014). "Force generation by endocytic actin patches in budding yeast." Biophys J **106**(8): 1596-1606.

13. Conner, S. D. and S. L. Schmid (2003). "Regulated portals of entry into the cell." Nature **422**(6927): 37-44.

14. Crick, S. L., K. M. Ruff, K. Garai, C. Frieden and R. V. Pappu (2013). "Unmasking the roles of N-and C-terminal flanking sequences from exon 1 of huntingtin as modulators of polyglutamine aggregation." Proceedings of the National Academy of Sciences **110**(50): 20075-20080.

15. Cross, R. (2012). "Elastic and viscous properties of Silly Putty." American Journal of Physics **80**: 870-875.

16. da Silva Pedrini, M. R., S. Dupont, A. de Anchieta Camara, Jr., L. Beney and P. Gervais (2014). "Osmoporation: a simple way to internalize hydrophilic molecules into yeast." Appl Microbiol Biotechnol **98**(3): 1271-1280.

17. Darwin, C. (1859). On the origin of species by means of natural selection, or, The preservation of favoured races in the struggle for life. London, J. Murray.

18. Das, R. K. and R. V. Pappu (2013). "Conformations of intrinsically disordered proteins are influenced by linear sequence distributions of oppositely charged residues." Proc Natl Acad Sci U

S A **110**(33): 13392-13397.

19. Derganc, J. and A. Copic (2016). "Membrane bending by protein crowding is affected by protein lateral confinement." Biochim Biophys Acta **1858**(6): 1152-1159.

20. Dill, K. A. and S. Bromberg (2011). Molecular driving forces : statistical thermodynamics in biology, chemistry, physics, and nanoscience. London ; New York, Garland Science.

21. Dmitrieff, S. and F. Nedelec (2015). "Membrane Mechanics of Endocytosis in Cells with Turgor." PLoS Comput Biol **11**(10): e1004538.

22. Elbaum-Garfinkle, S., Y. Kim, K. Szczepaniak, C. C. Chen, C. R. Eckmann, S. Myong and C. P. Brangwynne (2015). "The disordered P granule protein LAF-1 drives phase separation into droplets with tunable viscosity and dynamics." Proc Natl Acad Sci U S A **112**(23): 7189-7194.

23. Elkhatib, N., E. Bresteau, F. Baschieri, A. L. Rioja, G. van Niel, S. Vassilopoulos and G. Montagnac (2017). "Tubular clathrin/AP-2 lattices pinch collagen fibers to support 3D cell migration." Science **356**(6343).

24. Feric, M., N. Vaidya, T. S. Harmon, D. M. Mitrea, L. Zhu, T. M. Richardson, R. W. Kriwacki, R. V. Pappu and C. P. Brangwynne (2016). "Coexisting Liquid Phases Underlie Nucleolar Subcompartments." Cell **165**(7): 1686-1697.

25. Fischer, M., A. C. Richardson, S. N. Reihani, L. B. Oddershede and K. Berg-Sorensen (2010). "Active-passive calibration of optical tweezers in viscoelastic media." Rev Sci Instrum **81**(1): 015103.

26. Ford, M. G., I. G. Mills, B. J. Peter, Y. Vallis, G. J. Praefcke, P. R. Evans and H. T. McMahon (2002). "Curvature of clathrin-coated pits driven by epsin." Nature **419**(6905): 361-366.

27. Foty, R. A., C. M. Pfleger, G. Forgacs and M. S. Steinberg (1996). "Surface tensions of embryonic tissues predict their mutual envelopment behavior." Development **122**(5): 1611-1620.

28. Gleisner, M., B. Kroppen, C. Fricke, N. Teske, T. T. Kliesch, A. Janshoff, M. Meinecke and C. Steinem (2016). "Epsin N-terminal Homology Domain (ENTH) Activity as a Function of Membrane Tension." J Biol Chem **291**(38): 19953-19961.

29. Guilak, F., J. R. Tedrow and R. Burgkart (2000). "Viscoelastic properties of the cell nucleus." Biochem Biophys Res Commun **269**(3): 781-786.

30. Guo, M., A. J. Ehrlicher, M. H. Jensen, M. Renz, J. R. Moore, R. D. Goldman, J. Lippincott-Schwartz, F. C. Mackintosh and D. A. Weitz (2014). "Probing the stochastic, motor-driven properties of the cytoplasm using force spectrum microscopy." Cell **158**(4): 822-832.

31. Guo, M., A. J. Ehrlicher, S. Mahammad, H. Fabich, M. H. Jensen, J. R. Moore, J. J. Fredberg, R. D. Goldman and D. A. Weitz (2013). "The role of vimentin intermediate filaments in cortical and cytoplasmic mechanics." Biophys J **105**(7): 1562-1568.

32. Gupta, K., J. A. Donlan, J. T. Hopper, P. Uzdavinys, M. Landreh, W. B. Struwe, D. Drew, A. J. Baldwin, P. J. Stansfeld and C. V. Robinson (2017). "The role of interfacial lipids in stabilizing membrane protein oligomers." Nature **541**(7637): 421-424.

33. Harmandaris, V. A. and M. Deserno (2006). "A novel method for measuring the bending rigidity of model lipid membranes by simulating tethers." J Chem Phys **125**(20): 204905.

34. Helfrich, W. (1973). "Elastic properties of lipid bilayers: theory and possible experiments." Z Naturforsch C **28**(11): 693-703.

35. Hendricks, A. G. and Y. E. Goldman (2017). "Measuring Molecular Forces Using Calibrated Optical Tweezers in Living Cells." Methods Mol Biol **1486**: 537-552.

36. Hendricks, A. G., E. L. Holzbaur and Y. E. Goldman (2012). "Force measurements on cargoes in living cells reveal collective dynamics of microtubule motors." Proc Natl Acad Sci U S A **109**(45): 18447-18452.

37. Hertz, H. R. (1882). Ueber die Beruehrung elastischer Koerper (On Contact Between Elastic Bodies). Leipzig, Germany, 1895.

38. Hester, J. J. (2008). "The Crab Nebula: An astrophysical chimera." Annual Review of Astronomy and Astrophysics **46**: 127-155.

39. Ho, C. H., L. Magtanong, S. L. Barker, D. Gresham, S. Nishimura, P. Natarajan, J. L. Koh, J.

Porter, C. A. Gray, R. J. Andersen, G. Giaever, C. Nislow, B. Andrews, D. Botstein, T. R. Graham, M. Yoshida and C. Boone (2009). "A molecular barcoded yeast ORF library enables mode-of-action analysis of bioactive compounds." Nat Biotechnol **27**(4): 369-377.

40. Huh, W. K., J. V. Falvo, L. C. Gerke, A. S. Carroll, R. W. Howson, J. S. Weissman and E. K. O'Shea (2003). "Global analysis of protein localization in budding yeast." Nature **425**(6959): 686-691.

41. Hyman, A. A., C. A. Weber and F. Julicher (2014). "Liquid-liquid phase separation in biology." Annu Rev Cell Dev Biol **30**: 39-58.

42. Idrissi, F. Z., A. Blasco, A. Espinal and M. I. Geli (2012). "Ultrastructural dynamics of proteins involved in endocytic budding." Proc Natl Acad Sci U S A **109**(39): E2587-2594.

43. Idrissi, F. Z., H. Grotsch, I. M. Fernandez-Golbano, C. Presciatto-Baschong, H. Riezman and M. I. Geli (2008). "Distinct acto/myosin-I structures associate with endocytic profiles at the plasma membrane." J Cell Biol **180**(6): 1219-1232.

44. Jiang, H., S. Wang, Y. Huang, X. He, H. Cui, X. Zhu and Y. Zheng (2015). "Phase transition of spindle-associated protein regulate spindle apparatus assembly." Cell **163**(1): 108-122.

45. Johnson, K. L. K., K.;Roberts, A. D. (1971). "Surface energy and the contact of elastic solid." Proc. R. Soc. Lond. A. **324**: 301-313.

46. Kanshin, E., L. P. Bergeron-Sandoval, S. S. Isik, P. Thibault and S. W. Michnick (2015). "A cell-signaling network temporally resolves specific versus promiscuous phosphorylation." Cell Rep **10**(7): 1202-1214.

47. Khurana, R., C. Coleman, C. Ionescu-Zanetti, S. A. Carter, V. Krishna, R. K. Grover, R. Roy and S. Singh (2005). "Mechanism of thioflavin T binding to amyloid fibrils." J Struct Biol **151**(3): 229-238.

48. Koenderink, G. H., M. Atakhorrami, F. C. MacKintosh and C. F. Schmidt (2006). "High-frequency stress relaxation in semiflexible polymer solutions and networks." Phys Rev Lett **96**(13): 138307.

49. Kroschwald, S., S. Maharana, D. Mateju, L. Malinovska, E. Nuske, I. Poser, D. Richter and S. Alberti (2015). "Promiscuous interactions and protein disaggregases determine the material state of stress-inducible RNP granules." Elife **4**: e06807.

50. Kukulski, W., A. Picco, T. Specht, J. A. Briggs and M. Kaksonen (2016). "Clathrin modulates vesicle scission, but not invagination shape, in yeast endocytosis." Elife **5**.

51. Kukulski, W., M. Schorb, M. Kaksonen and J. A. Briggs (2012). "Plasma membrane reshaping during endocytosis is revealed by time-resolved electron tomography." Cell **150**(3): 508-520.

52. Kull, H. J. (1991). "Theory of the Rayleigh-Taylor Instability." Physics Reports-Review Section of Physics Letters **206**(5): 197-325.

53. Li, D., L. Shao, B. C. Chen, X. Zhang, M. Zhang and B. Moses (2015). "Extended-resolution structured illumination imaging of endocytic and cytoskeletal dynamics." Science (New York, NY).

54. Li, Y., R. Lipowsky and R. Dimova (2011). "Membrane nanotubes induced by aqueous phase separation and stabilized by spontaneous curvature." Proc Natl Acad Sci U S A **108**(12): 4731-4736.

55. Lieleg, O., K. M. Schmoller, M. M. Claessens and A. R. Bausch (2009). "Cytoskeletal polymer networks: viscoelastic properties are determined by the microscopic interaction potential of cross-links." Biophys J **96**(11): 4725-4732.

56. Lin, Y., D. S. W. Protter, M. K. Rosen and R. Parker (2015). "Formation and Maturation of Phase-Separated Liquid Droplets by RNA-Binding Proteins." Molecular Cell **60**(2): 208-219.

57. Mahadevi, A. S. and G. N. Sastry (2016). "Cooperativity in Noncovalent Interactions." Chem Rev **116**(5): 2775-2825.

58. Malinovska, L., S. Kroschwald and S. Alberti (2013). "Protein disorder, prion propensities, and self-organizing macromolecular collectives." Biochim Biophys Acta **1834**(5): 918-931.

59. Molliex, A., J. Temirov, J. Lee, M. Coughlin, A. P. Kanagaraj, H. J. Kim, T. Mittag and J. P.

628   Taylor (2015). "Phase separation by low complexity domains promotes stress granule assembly
629   and drives pathological fibrillization." Cell **163**(1): 123-133.

630 60. Munder, M. C., D. Midtvedt, T. Franzmann, E. Nuske, O. Otto, M. Herbig, E. Ulbricht, P.
631   Muller, A. Taubenberger, S. Maharana, L. Malinovska, D. Richter, J. Guck, V. Zaburdaev and S.
632   Alberti (2016). "A pH-driven transition of the cytoplasm from a fluid- to a solid-like state
633   promotes entry into dormancy." Elife **5**.

634 61. Nott, T. J., E. Petsalaki, P. Farber, D. Jervis, E. Fussner, A. Plochowietz, T. D. Craggs, D. P.
635   Bazett-Jones, T. Pawson, J. D. Forman-Kay and A. J. Baldwin (2015). "Phase transition of a
636   disordered nuage protein generates environmentally responsive membraneless organelles." Mol
637   Cell **57**(5): 936-947.

638 62. Pappu, R. V., X. Wang, A. Vitalis and S. L. Crick (2008). "A polymer physics perspective on
639   driving forces and mechanisms for protein aggregation." Arch Biochem Biophys **469**(1): 132-
640   141.

641 63. Picco, A., M. Mund, J. Ries, F. Nedelec and M. Kaksonen (2015). "Visualizing the functional
642   architecture of the endocytic machinery." Elife **4**.

643 64. Pietrosemoli, N., R. Pancsa and P. Tompa (2013). "Structural disorder provides increased
644   adaptability for vesicle trafficking pathways." PLoS Comput Biol **9**(7): e1003144.

645 65. Reichheld, S. E., L. D. Muiznieks, F. W. Keeley and S. Sharpe (2017). "Direct observation of
646   structure and dynamics during phase separation of an elastomeric protein." Proc Natl Acad Sci U
647   S A **114**(22): E4408-E4415.

648 66. Ries, J., C. Kaplan, E. Platonova, H. Eghlidi and H. Ewers (2012). "A simple, versatile method
649   for GFP-based super-resolution microscopy via nanobodies." Nat Methods **9**(6): 582-584.

650 67. Roman, B. and J. Bico (2010). "Elasto-capillarity: deforming an elastic structure with a liquid
651   droplet." J Phys Condens Matter **22**(49): 493101.

652 68. Scher-Zagier, J. K. and A. E. Carlsson (2016). "Local Turgor Pressure Reduction via Channel
653   Clustering." Biophys J **111**(12): 2747-2756.

654 69. Sheff, M. A. and K. S. Thorn (2004). "Optimized cassettes for fluorescent protein tagging in
655   Saccharomyces cerevisiae." Yeast **21**(8): 661-670.

656 70. Skruzny, M., A. Desfosses, S. Prinz, S. O. Dodonova, A. Gieras, C. Uetrecht, A. J. Jakobi, M.
657   Abella, W. J. H. Hagen, J. Schulz, R. Meijers, V. Rybin, J. A. G. Briggs, C. Sachse and M.
658   Kaksonen (2015). "An Organized Co-assembly of Clathrin Adaptors Is Essential for
659   Endocytosis." Developmental Cell **33**(2): 150-162.

660 71. Style, R. W., C. Hyland, R. Boltyanskiy, J. S. Wettlaufer and E. R. Dufresne (2013). "Surface
661   tension and contact with soft elastic solids." Nat Commun **4**: 2728.

662 72. Tallinen, T., J. Chung, F. Rousseau, N. Girard, J. Lefèvre and L. Mahadevan (2016). "On the
663   growth and form of cortical convolutions." Nature Physics **12**: 588–593.

664 73. Tarassov, K., V. Messier, C. R. Landry, S. Radinovic, M. M. Serna Molina, I. Shames, Y.
665   Malitskaya, J. Vogel, H. Bussey and S. W. Michnick (2008). "An in vivo map of the yeast protein
666   interactome." Science **320**(5882): 1465-1470.

667 74. Thompson, D. A. W. (1917). On growth and form. Cambridge Eng., University press.

668 75. Toombs, J. A., B. R. McCarty and E. D. Ross (2009). "Compositional Determinants of Prion
669   Formation in Yeast." Molecular and Cellular Biology **30**(1): 319-332.

670 76. Updike, D. L., S. J. Hachey, J. Kreher and S. Strome (2011). "P granules extend the nuclear pore
671   complex environment in the C. elegans germ line." J Cell Biol **192**(6): 939-948.

672 77. Watson, H. A., M. J. Cope, A. C. Groen, D. G. Drubin and B. Wendland (2001). "In vivo role for
673   actin-regulating kinases in endocytosis and yeast epsin phosphorylation." Mol Biol Cell **12**(11):
674   3668-3679.

675 78. Wei, M.-T., S. Elbaum-Garfinkle, A. S. Holehouse, C. C.-H. Chen, M. Feric, C. B. Arnold, R. D.
676   Priestley, R. V. Pappu and C. P. Brangwynne (2017). "Phase behaviour of disordered proteins
677   underlying low density and high permeability of liquid organelles." NATURE CHEMISTRY.

678 79. Wheeler, J. R., T. Matheny, S. Jain, R. Abrisch and R. Parker (2016). "Distinct stages in stress

679 granule assembly and disassembly." <u>Elife</u> **5**.

680 **80.** Xi, K., T. Byrnes and H. Saito (2017). "Fingering instabilities and pattern formation in a two-
681 component dipolar Bose-Einstein condensate." <u>arXiv</u> **1704.04949v1**

682 81. Youn, J. Y., H. Friesen, T. Kishimoto, W. M. Henne, C. F. Kurat, W. Ye, D. F. Ceccarelli, F.
683 Sicheri, S. D. Kohlwein, H. T. McMahon and B. J. Andrews (2010). "Dissecting BAR domain
684 function in the yeast Amphiphysins Rvs161 and Rvs167 during endocytosis." <u>Mol Biol Cell</u>
685 **21**(17): 3054-3069.

686 82. Yu, H. and K. Schulten (2013). "Membrane sculpting by F-BAR domains studied by molecular
687 dynamics simulations." <u>PLoS Comput Biol</u> **9**(1): e1002892.

688 83. Zhang, H., S. Elbaum-Garfinkle, E. M. Langdon, N. Taylor, P. Occhipinti, A. A. Bridges, C. P.
689 Brangwynne and A. S. Gladfelter (2015). "RNA Controls PolyQ Protein Phase Transitions."
690 <u>Molecular Cell</u> **60**(2): 220-230.

691 84. Zhang, W., P. Soman, K. Meggs, X. Qu and S. Chen (2013). "Tuning the Poisson's Ratio of
692 Biomaterials for Investigating Cellular Response." <u>Adv Funct Mater</u> **23**(25): 3226-3232.

693 85. Zhao, H., A. Michelot, E. V. Koskela, V. Tkach, D. Stamou, D. G. Drubin and P. Lappalainen
694 (2013). "Membrane-sculpting BAR domains generate stable lipid microdomains." <u>Cell Rep</u> **4**(6):
695 1213-1223.

696